remote sensing

MDPI

Article

Effects of Assimilating Ground-Based Microwave Radiometer and FY-3D MWTS-2/MWHS-2 Data in Precipitation Forecasting

Bingli Wang [1,2], Wei Cheng [3], Yansong Bao [1,2,*], Shudong Wang [4], George P. Petropoulos [5], Shuiyong Fan [6], Jiajia Mao [7], Ziqi Jin [8] and Zihui Yang [9]

1 Collaborative Innovation Center on Forecast and Evaluation of Meteorological Disasters, China Meteorological Administration Key Laboratory for Aerosol-Cloud-Precipitation, Nanjing University of Information Science & Technology, Nanjing 210044, China; 20211205019@nuist.edu.cn
2 School of Atmospheric Physics, Nanjing University of Information Science and Technology, Nanjing 210044, China
3 Beijing Institute of Applied Meteorology, Beijing 100029, China; chengw@mail.iap.ac.cn
4 Public Meteorological Service Center of China Meteorological Administration, Beijing 100081, China; wsd@mail.iap.ac.cn
5 Department of Geography, Harokopio University of Athens, EI. Venizelou 70, 17671 Athens, Greece; gpetropoulos@hua.gr
6 Institute of Urban Meteorology, China Meteorological Administration, Beijing 100089, China; syfan@ium.cn
7 Meteorological Observation Center of China Meteorological Administration, Beijing 100081, China; maojj@cma.gov.cn
8 Zhejiang Institute of Meteorological Sciences, Hangzhou 310008, China; 20191205003@nuist.edu.cn
9 Nanjing University of Information Science & Technology, Nanjing 210044, China; 20211201143@nuist.edu.cn
* Correspondence: ysbao@nuist.edu.cn

Abstract: This study investigates the impacts of the joint assimilation of ground-based microwave radiometer (MWR) and FY-3D microwave sounder (MWTS-2/MWHS-2) observations on the analyses and forecasts for precipitation forecast. Based on the weather research and forecasting data assimilation (WRFDA) system, four experiments are conducted in this study, concerning a heavy precipitation event in Beijing on 2 July 2021, and 10-day batch experiments were also conducted. The key study findings include the following: (1) Both ground-based microwave radiometer and MWTS-2/MWHS-2 data contribute to improvements in the initial fields of the model, leading to appropriate adjustments in the thermal structure of the model. (2) The forecast fields of the experiments assimilating ground-based microwave radiometer and MWTS-2/MWHS-2 data show temperature and humidity performances closer to the true fields compared with the control experiment. (3) Separate assimilation of two types of microwave radiometer data can improve precipitation forecasts, while joint assimilation provides the most accurate forecasts among all the experiments. In the single-case, compared with the control experiment, the individual and combined assimilation of MWR and MWTS-2/MWHS-2 improves the six-hour cumulative precipitation threat score (TS) at the 25 mm level by 57.1%, 28.9%, and 38.2%, respectively. The combined assimilation also improves the scores at the 50 mm level by 54.4%, whereas individual assimilations show a decrease in performance. In the batch experiments, the MWR_FY experiment's TS of 24 h precipitation forecast improves 28.5% at 10 mm and 330% at 25 mm based on the CTRL.

Keywords: FY-3D MWTS-2/MWHS-2; ground-based microwave radiometer; data assimilation

Citation: Wang, B.; Cheng, W.; Bao, Y.; Wang, S.; Petropoulos, G.P.; Fan, S.; Mao, J.; Jin, Z.; Yang, Z. Effects of Assimilating Ground-Based Microwave Radiometer and FY-3D MWTS-2/MWHS-2 Data in Precipitation Forecasting. *Remote Sens.* **2024**, *16*, 2682. https://doi.org/10.3390/rs16142682

Academic Editor: Gyuwon Lee

Received: 16 May 2024
Revised: 25 June 2024
Accepted: 16 July 2024
Published: 22 July 2024

1. Introduction

The accuracy of numerical weather prediction (NWP) is heavily reliant on the quality of its initial conditions, prompting a growing focus on data assimilation to enhance these foundational elements. Satellite data such as infrared radiation data, microwave detection data, satellite precipitation data, etc., play a crucial role in this context due to their comprehensive coverage and advantages in observational sources [1–3]. Extensive

research evidences that satellite observations significantly refine the initial model fields, thereby elevating forecast precision [4–7]. Currently, satellite data comprise over 90% of the observational inputs utilized by numerical prediction centers globally, underscoring the critical contribution to the advancement of NWP [8]. The superior spatial and temporal resolution of satellite observations, along with their capability to bridge the observational gaps in complex terrains and maritime domains, solidifies their indispensable status in improving weather forecasting accuracy [9].

Microwave remote sensing is particularly valuable for its ability to penetrate clouds and precipitation, providing critical data on weather systems. Microwave detection technologies enable enhanced observation of cloud regions, which is crucial for analyzing and forecasting weather systems [10]. Both microwave vertical sounders and imagers are integral to data assimilation systems, earning them widespread application in meteorological research and operations [11–14].

FY-3D, China's second-generation polar orbit meteorological satellite, features the upgraded microwave temperature sounder (MWTS-2) and microwave humidity sounder (MWHS-2), improving upon its predecessors MWTS/MWHS with channel configurations and observational accuracy akin to the AMSU-A of Europe and America [15]. Regarding the Fengyun-3 satellite series, scholars have conducted extensive research on its microwave vertical detector. In analyzing the detection data from the FY-3A satellite, researchers have observed that, although the deviation in its microwave hygrometer readings is somewhat larger, the overall data quality is on par with that of international instruments, especially in terms of the global average [16–19]. In the follow-up assimilation experiments involving the FY-3 series satellites, the substantial enhancements in numerical predictions facilitated by microwave data have been progressively unveiled. Chen et al. [20] integrated the microwave hygrometer data from FY-3A/3B (MWHS) into the assimilation system of the European Centre for Medium-Range Weather Forecasts (ECMWF). Their findings demonstrated that these data not only enhanced the model's analysis field but also had a forecast impact on par with that of similar long-term used foreign instruments. Subsequently, ECMWF formally integrated observations from the FY-3B microwave hygrometer over oceanic regions into its operational forecasting model in 2014. In 2015, Lawrence [21] and Lu et al. [22] initiated evaluations of the FY-3C microwave hygrometer (MWHS-2) data quality, conducting tests within both the Met Office and the ECMWF assimilation systems. Their findings indicated that the quality of the 183 GHz channel data was comparable to that of ATMS and MHS instruments. Importantly, the inclusion of these channel data had a positive impact on humidity predictions in short-term forecasts, with MWHS-2 achieving a significant 6% reduction in 24 h forecast errors in the Met Office's global model. In another study, Xu et al. [5] examined the assimilation effects of the FY-3B microwave hygrometer (MWHS) during a binary typhoon event (Chan-hom and Linfa), observing corrections in both the location and magnitude of predicted precipitation over 24 h. The study employed two assimilation strategies—three-dimensional variation and mixed variation—which were later adopted by Sun et al. [23] in their assessment of MWHS-2 data assimilation on Typhoon Ampil. Their results demonstrated that MWHS-2 data enhanced not only precipitation accumulation predictions but also its evolutionary characteristics. Other studies, such as those by Song et al. [24], Xu et al. [25], and Chen et al. [26], assimilated FY-3D MWHS-2 data to forecast typhoon events, and the results showed that the data had a positive impact on typhoon track prediction. Current research underscores the critical role of assimilating FY-3D microwave detector data in enhancing initial model fields and forecast accuracy, which has significant potential for elevating the technical capability of NWP, particularly for short- to medium-term forecasts.

Ground-based microwave radiometers, similar to satellite microwave sensors, passively capture atmospheric temperature and humidity information through microwave radiation. These radiometers offer continuous all-weather observations with high spatiotemporal resolution without the need for manual operation. This advantage effectively overcomes the limitations of spatial and temporal resolution in sounding data and com-

pensates for the shortcomings of satellite data in detecting the planetary boundary layer. Numerous international studies have explored their application in numerical weather prediction. Vandenberghe and Ware [27] performed both three-dimensional and four-dimensional variational assimilation experiments using ground-based microwave radiometer data for winter fog events, demonstrating the potential of data assimilation to predict fog formation. Similarly, Otkin et al. [28] and Hartung et al. [29], using observing system simulation experiments (OSSEs) for a winter storm scenario, found that assimilating data at the ground remote sensing stations, including microwave radiometers, positively influenced temperature and humidity analyses. Caumont et al. [30] integrated temperature and humidity data from microwave radiometer stations into a convective-scale NWP, demonstrating beneficial results from MWR data assimilation. Martinet et al. [31,32] incorporated MWR observation data into the AROME (application of research to operations at mesoscale) model using a one-dimensional variational (1D-VAR) retrieval technique. This approach notably improved the model's forecast accuracy within a 3 km range and effectively captured near-surface temperatures. Furthermore, the Swiss Federal Office of Meteorology and Climatology (MeteoSwiss) and the Deutscher Wetterdienst (DWD) collaborated to utilize MWR data for refining the initial conditions of the atmospheric boundary layer (ABL). They employed RTTOV-gb (radiative transfer for TIROS operational vertical sounder, ground-based) for the direct assimilation of MWR emissivity. In MeteoSwiss, observations from two MWR stations indicated a positive impact on temperature accuracy. DWD conducted assimilation tests with different schemes, including single-channel and multi-channel selections, which further confirmed MWR's positive influence on ABL temperature and humidity forecasts [33].

Current research indicates that both ground-based microwave radiometers and FY-3D satellite observations from MWTS-2/MWHS-2 data have significant potential for advancing numerical prediction technologies. However, the data assimilation research on the microwave data of the FY-3D satellite is not yet sufficient, especially the assimilation of all-sky data combining temperature and humidity sensors [23–26]. Similarly, although some scholars have conducted some forecasting studies on ground-based microwave radiometers, the application of ground-based microwave radiometers in data assimilation is still in its early stages compared with the assimilation of satellite microwave data, and the research is focused mainly on regions outside of China, with very few studies specifically targeting the Chinese region [27–36]. Based on the above, this paper analyzes and forecasts a short-term heavy precipitation event in Beijing using ground-based microwave radiometers and FY-3D MWTS-2/MWHS-2 data. By conducting comparative experiments, the study explores the impact of these two types of data on precipitation in the Beijing region.

In purview of the above, the present study aims at exploring the independent and combined impacts of these two microwave data sources on regional NWP assimilation and forecasting to improve precipitation forecast accuracy in the Beijing area. Additionally, it provides valuable references for the application of these two types of data in numerical weather forecast models. This study is structured as follows: An introduction to the ground-based microwave radiometer and FY-3D MWTS-2/MWHS-2 is presented in Section 2, along with the preprocessing specific to these datasets. In Section 3, the experiments' design and an introduction to individual precipitation cases are introduced. Section 4 showcases and discusses the results of numerical experiments, whereas Section 5 provides the study conclusions and some final remarks.

2. Datasets and Preprocessing

2.1. Ground-Based Microwave Radiometer and Preprocessing

The ground-based microwave radiometer data used in this study are from the megacity comprehensive observation experiment. Observation stations located in the Beijing area from July to August 2021 were selected. There are six stations in total, namely Haidian (Station ID 54399), Yanqing (Station ID 54406), Huairou (Station ID 54419), Pinggu (Station ID 54424), Nanjiao (Station ID 54511), and Xiayunling (Station ID 54597), as shown in

Figure 1. Each ground-based microwave radiometer has 14 receiving channels, including seven temperature channels (52.26 to 58.00 GHz) and seven humidity channels (22.24 to 31.40 GHz). These radiometers can observe the atmosphere from the surface up to an altitude of 10 km, with a temporal resolution of 2 min. The generated data products include LV1 class brightness temperature and LV2 class retrieval products, offering profiles of temperature and relative humidity. The profiles have 83 height levels, with resolutions of 25 m from 0 to 0.5 km, 50 m from 0.5 to 2 km, and 250 m from 2 to 10 km altitudes.

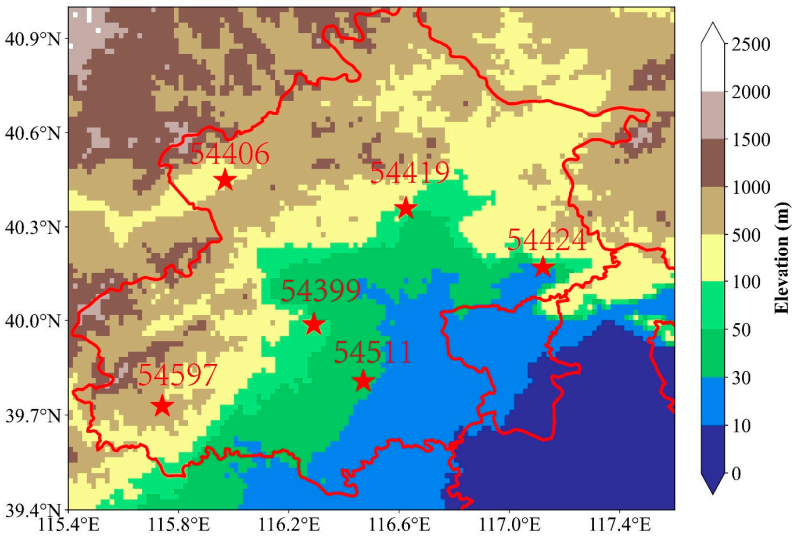

Figure 1. Distribution of ground microwave radiometer stations, located in Beijing, China: Haidian (Station ID 54399), Yanqing (Station ID 54406), Huairou (Station ID 54419), Pinggu (Station ID 54424), Nanjiao (Station ID 54511), and Xiayunling (Station ID 54597).

Ground-based microwave radiometers have the potential to supplement or even replace data traditionally obtained by sounding balloons, due to advancements in remote sensing technology that have brought their measurement accuracy closer to that of radiosonde data. Studies have shown a statistically significant correlation between ground-based radiometer measurements of temperature, water vapor density, and relative humidity with radiosonde observations [37–39]. In this study, data from a radiosonde station in the Beijing area (Station ID 54511) and retrieval products from a collocated ground-based microwave radiometer were analyzed over a month, as shown in Table 1. The findings indicated significant correlations, with temperature and specific humidity correlation coefficients exceeding 0.9 and relative humidity around 0.75, while maintaining the mean bias within 1. These results underscore the critical role of ground-based microwave radiometers in atmospheric detection and their promising application prospects. Although ground-based microwave radiometers have not been widely used, their potential and contribution to improving weather forecasting accuracy deserve further exploration and evaluation through more extensive experimental research.

Before entering the assimilation system, quality control (QC) and bias correction (BC) of temperature and humidity profiles of ground-based microwave radiometer retrieval products were performed. To ensure unbiased entry of these profiles into the assimilation system, ERA5 (reanalysis data from the ECMWF) [40] three-hour forecast data served as the reference during the preprocessing. Firstly, calculate the standard deviation (σ) of all the data deviations. Remove data points with deviations exceeding three times the standard deviation. Subsequently, employ a univariate linear model to perform bias correction on the data. Taking the temperature profile as an example, Figure 2 shows the probability distribution function of the bias of temperature data at six stations before and after QC and BC. As can be seen from the red shading and the red curve, the mean bias of the temperature is larger before QC and BC. After preprocessing, the mean bias of each station

decreased and tended to zero, and the probability distribution functions approached a Gaussian distribution.

Table 1. Overall temperature and relative humidity evaluation results from ground-based microwave radiometer and radiosonde at Station 54511. RMSE—root mean square error.

Element	Evaluation Index	Index Value
Temperature	Bias/K	−0.4053
	RMSE/K	1.968
	Correlation coefficient	0.994
Relative humidity	Bias/%	0.642
	RMSE/%	11.23
	Correlation coefficient	0.7515
Specific humidity	Bias/(g/kg)	−0.01768
	RMSE/(g/kg)	1.413
	Correlation coefficient	0.9717

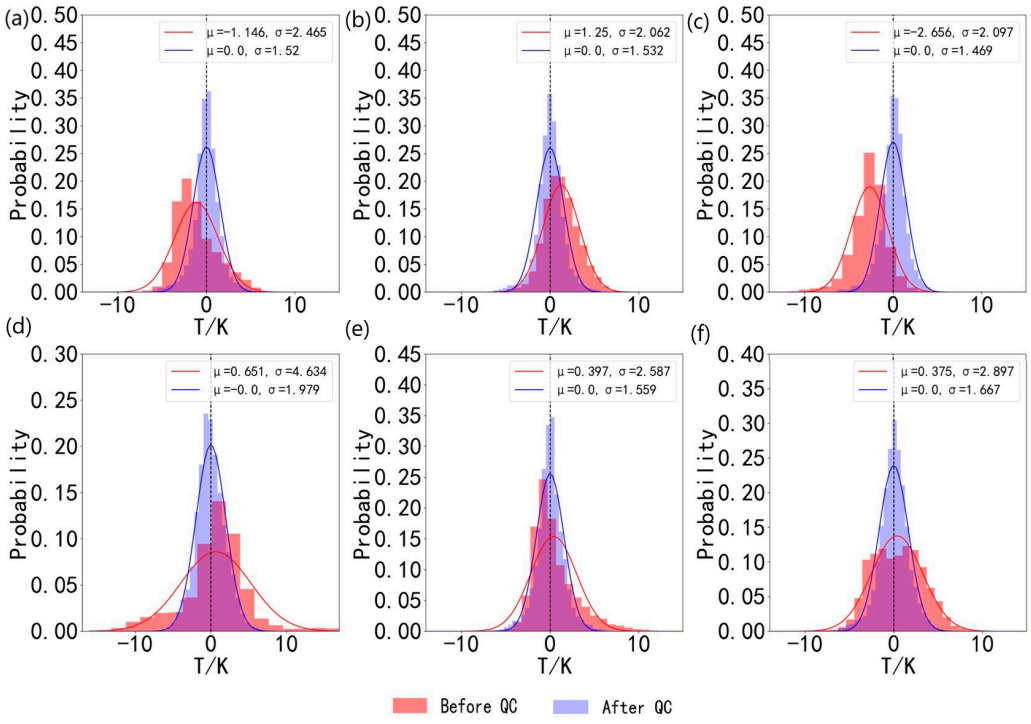

Figure 2. Probability distribution function of deviations in ground-based microwave radiometer temperature data before and after preprocessing for stations (**a**) 54511, (**b**) 54597, (**c**) 54419, (**d**) 54424, (**e**) 54511, and (**f**) 54597. The red "u" and "o" represent the error mean and error standard deviation of all samples before QC and BC. The blue "u" and "o" represent the error mean and error standard deviation of all samples after QC and BC.

2.2. FY-3D MWTS-2/MWHS-2 and Preprocessing

2.2.1. FY-3D MWTS-2/MWHS-2

The FY-3D satellite is the fourth second-generation polar-orbiting satellite launched by China. Its orbit is about 830 km above the Earth, and it can detect the same area of the Earth twice a day. MWTS-2 has a total of 13 detection channels at 50 to 60 GHz and is capable of receiving ground information and vertical temperature distribution from the surface to the atmosphere at an altitude of 3 hPa. The instrument has an orbital width of 2250 km and produces 14 observational data files per day, generating a total of 14 passes daily. Each file has 1212 scan lines, with each scan line having 90 ground observation pixels. The instrument has a nadir resolution of 33 km.

MWHS-2 has 15 detection channels, of which several channels with a center frequency of 118 GHz are oxygen absorption channels, which are mainly used to detect the vertical distribution of atmospheric temperature. Several channels with a center frequency of 183 GHz are mainly used to detect the vertical distribution of atmospheric humidity. Channels 1 and 10 are window channels used to detect ground information. The instrument has an orbital width of 2260 km and produces 14 observational data files per day. Each file has 2378 scan lines, with each scan line having 98 ground observation pixels. The nadir resolution of channels 1 to 9 is 32 km, while the nadir resolution of channels 10 to 15 is 16 km.

2.2.2. Quality Control

Since satellite observation data can be affected by factors related to the instruments and the detection environment, directly integrating these data into assimilation systems can introduce significant errors [41]. It is necessary to eliminate data of poor quality and low precision to ensure the quality of the assimilated materials. For the quality control of MWTS-2/MWHS-2, existing research has already summarized a set of mature quality control schemes. This paper's specific approach includes the following items:

(1) Observations with MWTS-2 brightness temperature less than 50 K and greater than 350 K are excluded, and the observations with MWHS-2 brightness temperature less than 90 K and greater than 340 K are excluded. Values that are too small or too large are not normal observations.
(2) Eliminate all observation data that contain mixed surface types, including mixed surface observations of ocean, sea ice, land, and snow.
(3) The zenith angle at the edges of the scan lines of the microwave detector is larger, resulting in a longer atmospheric radiation path and consequently lower observed radiance values. Therefore, observations from the five scanning points on both the left and right sides of each scan line of MWTS-2 are eliminated, as well as observations from the six scanning points on both the left and right sides of each scan line of MWHS-2.
(4) Eliminate observations with residuals (observation minus background, O-B) exceeding three times the standard deviation of the residual values.
(5) Eliminate channel observations for viewpoints located in cloudy areas. The method for cloud detection is based on cloud detection products from the moderate resolution spectral imager (MERSI) on the same satellite. By matching the field of view angles of the two types of data, if the average cloud cover within the instantaneous field of view of the microwave detector is greater than 76% [42], then that viewpoint is considered a cloudy area.
(6) Considering the impact of surface factors and the limitations of model altitude, the assimilation experiment selects MWTS-2 channels 4 to 9 and MWHS-2 channels 11 to 13 and channel 15, excluding the window region and upper atmosphere. Channel 14 of MWHS-2 is not selected due to its significant errors [43].
(7) To minimize potential correlations between adjacent radiance observations, the MWTS-2/MWHS-2 radiance data are thinned on a 45 km grid.

2.2.3. Bias Correction

Due to multiple sources of error, such as instrument sensitivity, sensor response characteristics, calibration, and radiative transfer models, there can be a systematic bias between satellite-observed brightness temperatures and the background field-simulated brightness temperatures [44]. After quality control, it is still necessary to correct the systematic bias between satellite-observed brightness temperatures and the model background fields to ensure that MWTS-2/MWHS-2 data enter the assimilation system with minimal bias. The variational bias correction (VarBC) module within the WRFDA assimilation system is used to correct biases for MWTS-2/MWHS-2. The radiance bias of satellite observations can be

represented by a linear combination of a set of forecast predictors pi, and the observation operator after bias correction $\widetilde{H}$ can be expressed as:

$$\widetilde{H}(x, \beta) = H(x) + \beta_0 + \sum_{i=1}^{N_p} \beta_i p_i \quad (1)$$

$H(x)$ is the observation operator before correction, β_0 is constant the deviation part, β_i and p_i are, respectively, the deviation correction factor and the forecasting factor. It is generally believed that the deviation correction coefficient is independent among channels, and the deviation correction coefficient can be obtained by off-line statistical calculation using the variational deviation correction method. This study utilizes observations from MWTS-2/MWHS-2 spanning from 1 July to 31 July 2021 to statistically derive bias correction coefficients, which are then applied in the current experiment.

Figure 3 shows the probability distribution function of observation-minus-background (OMB) and observation-minus-analysis (OMA) for MWTS-2 channel 7 and MWHS-2 channel 11 before and after bias correction at 1800 UTC on 1 July 2021. The analysis is based on clear-sky observations post-quality control. There is a significant negative bias for the two channels before correction. After correction, the mean bias is close to zero, and the root mean square error (RMSE) is notably reduced. The OMA distribution indicates that the mean bias between the analysis field and observation is close to zero. These findings demonstrate that systematic biases in satellite observation data are effectively minimized following quality control and bias correction, ensuring the reliability of data entering the assimilation system.

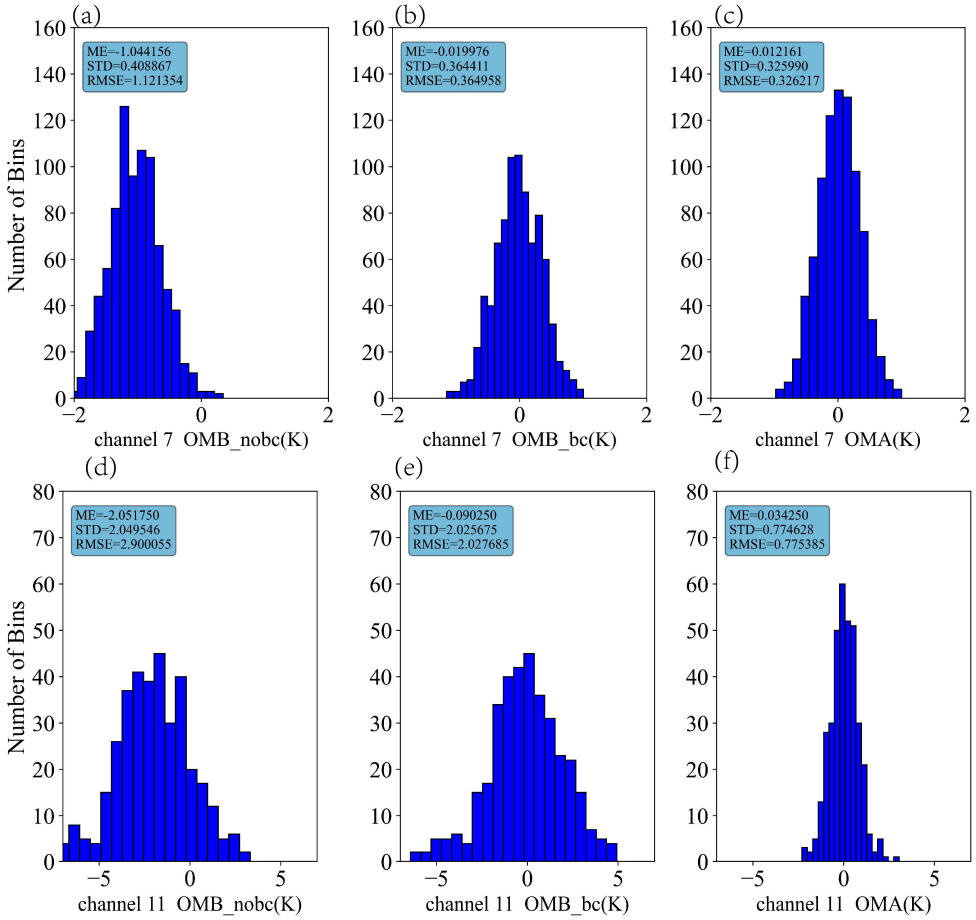

Figure 3. Probability distribution function of observation-minus-background (OMB) for (**a**,**d**) without bias correction, (**b**,**e**) OMB with bias correction, and (**c**,**f**) OMA with bias correction of (**a**–**c**) MWTS-2 ch7, (**d**–**e**) MWHS-2 ch11, respectively. "ME" represents the mean, "STD" represents the standard deviation, and "RMSE" represents the root-mean-square error.

2.2.4. Retrieval of Satellite Emissivity in the Cloud Region

To comprehensively assess the role of MWTS-2/MWHS-2 data in data assimilation, this study not only investigates data assimilation under clear-sky conditions but also considers observations under cloudy conditions. The data under cloudy conditions are initially processed using the retrieve method, followed by assimilating the retrieval temperature and humidity profiles. This study employs an artificial neural network (ANN) algorithm for retrieval, a technique that has been widely applied in remote sensing data retrieval and has reached a mature stage of application [45,46]. Jin et al. [47] successfully applied the ANN algorithm for the classification retrieval and assimilation of brightness temperature data in the cloud regions of MWTS-2/MWHS-2, yielding significant outcomes. This paper adopts its retrieve method. The advantages of this method include direct use of the observed brightness temperature for modeling, avoiding the need for bias correction of brightness temperature in the retrieve process; the forward derivation of the neural network can be completed offline without relying on any additional input data; and the data error obtained from the retrieval is not affected by the background field.

In constructing the neural network model for this study, ERA5 reanalysis data with a spatial resolution of $0.1^\circ \times 0.1^\circ$ are combined with satellite-observed brightness temperature data to create a training sample database. Utilizing the cloud detection method described above, cloud samples from May 2021 are identified and categorized by surface type (marine and land) over China and its adjacent regions. The artificial neural network is designed with a four-layer architecture, comprising an input layer, two hidden layers, and an output layer. The model has 30 nodes in the hidden layers for temperature retrieval and 35 nodes for humidity retrieval. The input layer's data include brightness temperature from the microwave detector, satellite zenith angle, and scan position information, with altitude and surface reflectivity data also included for land areas. The output layer generates temperature and humidity profiles, which have 37 height levels. In this neural network model, the activation function employed between each layer is the hyperbolic tangent sigmoid transfer function (tansig). The "tansig" function maps the input values into a range between -1 and 1, and its nonlinear characteristics enable the network to adeptly learn and simulate the complex relationships between input and output data. The training algorithm used for the neural network is the conjugate gradient method. This method optimizes the network weights by adjusting the direction and step length of the gradient descent, aiming to minimize the error function. It is known for its rapid convergence and stable performance, making it especially suitable for addressing large-scale network challenges.

Figure 4 shows the cloud distribution after cloud matching at 1800 UTC on 1 July (Figure 4a) and 0600 UTC on 2 July (Figure 4b) and the cloud cover distribution from the moderate resolution spectral imager (MERSI) carried by the FY-3D satellite (Figure 4c,d). The comparison between cloud matching and observational data reveals a strong correspondence in both cloud and clear-sky regions, demonstrating the effectiveness of the cloud matching method. The proportion of cloud-covered areas is substantial; thus, the effective utilization of satellite cloud data is of significant importance for the advancement of numerical forecasting. Figure 5 shows the distribution of clear-sky observations from channel 11 of MWHS-2 at 1800 UTC on 1 July (Figure 5a,b) and 0600 UTC on 2 July (Figure 5c,d) and temperature retrieval data at the 500 hPa altitude. In the Beijing region, predominantly clear-sky observations are observed at 1800 on 1 July, with partial cloud retrieval data observed at 0600 on 2 July.

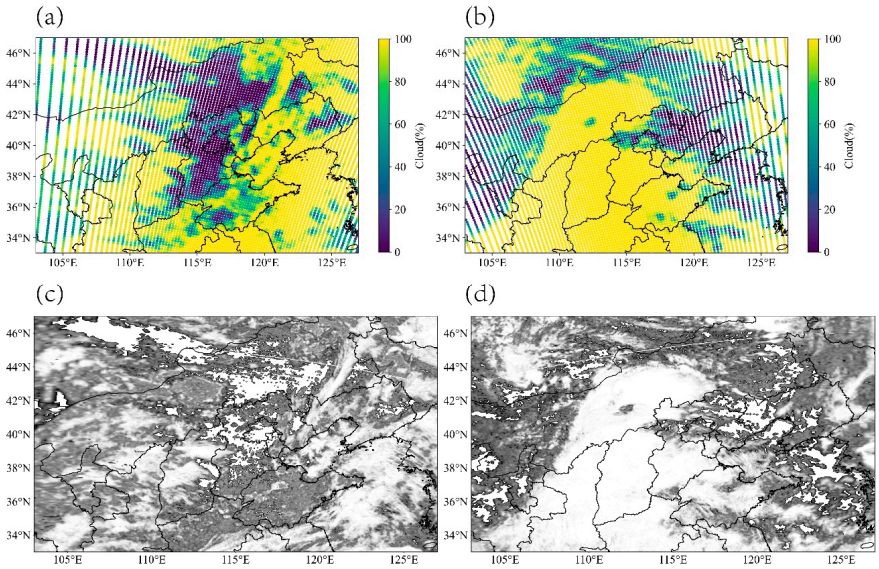

Figure 4. Cloud distribution after cloud matching (**a**,**b**) and true cloud distribution from the moderate resolution spectral imager (MERSI) (**c**,**d**) at 1800 UTC on 1 July (**a**,**c**) and 0600 UTC on 2 July (**b**,**d**).

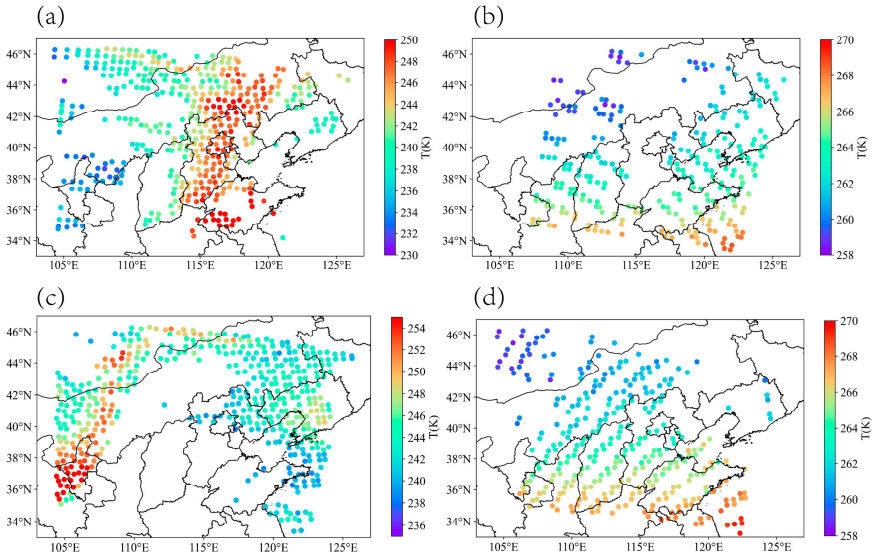

Figure 5. Brightness temperature distribution in MWTS-2 channel 11 under clear-sky conditions (**a**,**c**) and retrieval temperature distribution at 500 hPa latitude (**b**,**d**) at 1800 UTC on 1 July (**a**,**b**) and 0600 UTC on 2 July (**c**,**d**).

3. Experiment Description and Model Configurations

3.1. Brief Description of Precipitation Case

In July 2021, the national average precipitation in China was 3.2% above the norm for the same period in previous years [48], with several regions experiencing more than 200 mm. In particular, the Beijing area encountered a significant precipitation event in early July, as shown in this case study. The precipitation mainly occurred from 1800 UTC on 2 July to 0000 UTC on 3 July (Figure 6), with the peak rainfall in the first three hours (Figure 6b) exceeding 50 mm, reaching storm level. The primary precipitation center was located in central Beijing and the confluence areas of Beijing, Tianjin, and Hebei, with the rain band extending from northeast to southwest across central Beijing. Subsequently, the precipitation center shifted eastward until the rainfall subsided. Characterized by high intensity and concentrated duration, this event represented a typical heavy precipitation occurrence.

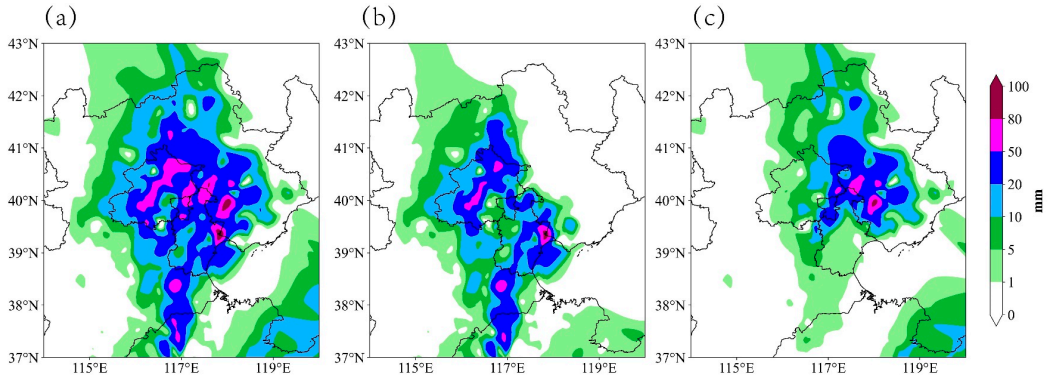

Figure 6. Distribution of cumulative precipitation in Beijing on 2 July 2021 (**a**) from 1800 UTC to 0000 UTC; (**b**) from 1800 UTC to 2100 UTC; (**c**) from 2100 UTC to 0000 UTC.

3.2. Model Configurations

This study uses the weather research and forecasting (WRF) model and the WRF data assimilation (WRFDA) system, developed by the National Center for Atmospheric Research (NCAR), and uses the RTTOV12.2 fast radiative transfer model serving as the observation operator to assimilate satellite radiance data. There are three assimilation schemes in the WRFDA assimilation system: three-dimensional variational (3D-Var) assimilation, four-dimensional variational (4D-Var) assimilation, and hybrid assimilation techniques. Specifically, this study selects the 3D-Var scheme, which uses the conjugate gradient method to minimize the cost function to obtain the optimal solution of the atmospheric state.

The research area center of the experiment was (40.16°N, 114.36°E), which mainly covered North China (Figure 7). The number of zonal and meridional grids in the test area were 424 and 550, respectively, with a horizontal resolution of 3 km. The model's vertical layers were set to 59, with a topmost pressure at 10 hPa. Physical parameterizations included the WSM6 microphysics scheme [49], RRTM long-wave radiation scheme [50], Goddard short-wave radiation scheme [51], Noah land surface [52], Monin–Obukhov near-surface scheme [53], Kain–Fritsch cumulus cloud scheme [54], and the Yonsei University boundary layer scheme [49]. The National Centers for Environmental Prediction (NCEP) global forecast system (GFS) analysis and forecasts were used to provide the background and boundary conditions. To address "spin up", the initial condition was derived from a 12 h integration of GFS data from 0600 UTC on 1 July. Assimilation and prediction were performed three separate times, with the assimilation data first added at 1800 UTC on 1 July and then the last assimilation at 0600 UTC on 2 July (Figure 8). The time window for assimilation was set to 2 h and the thinning distance of MWTS-2/MWHS-2 radiance data was 45 km.

This study set four experiments. The first experiment assimilated only conventional observational data, which included ground station data from global communication systems, radiosondes, aircraft, and ship observations, and this setup was referred to as CTRL. In the second set of experiments, the temperature and humidity profiles of the ground-based microwave radiometer were added based on conventional observation data, and were recorded as MWR. The third set of tests was based on the CTRL, and the MWTS-2/MWHS-2 data were added at the moment of 1800 UTC and 0600 UTC of the FY-3D satellites passing through the experiment area, respectively, and were recorded as FY. The fourth experiment combined the MWR and FY experiments, joined the conventional observation, ground-based microwave radiometer, and MWTS-2/MWHS-2 data into the assimilation system, and were recorded as MWR_FY. When assimilating conventional observations, the CV3 scheme was employed as the background error covariance, while, for assimilating other datasets, the CV7 scheme was used [55].

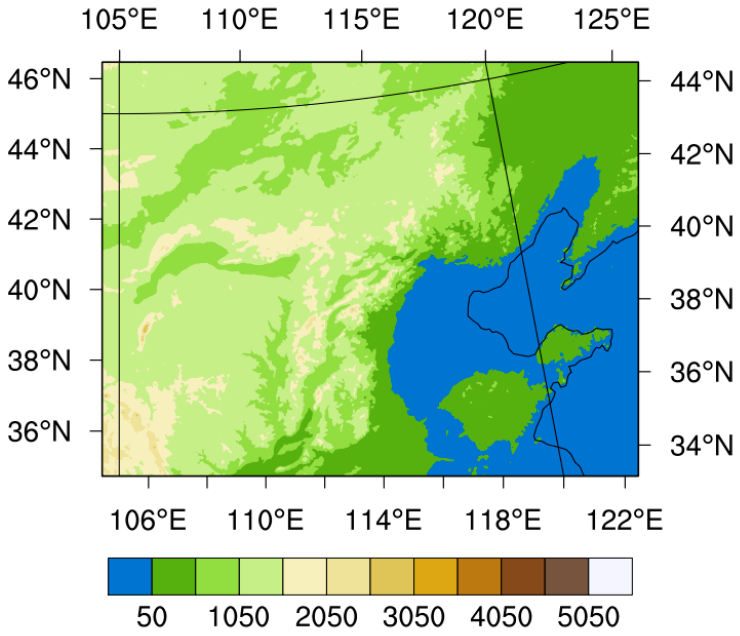

Figure 7. Simulated area in ARW-WRF.

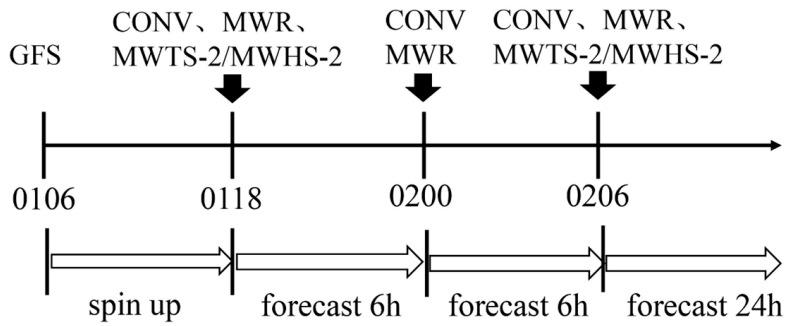

Figure 8. Assimilation flowchart.

3.3. Batch Experiments

In addition to the single-case experiment using cyclic assimilation, the study used batch experiments to verify the effect of microwave data on assimilation forecasts. The batch experiment used the single assimilation plus forecast method, and 10-day batch experiments were conducted, specifically from 1 to 10 July 2021. That is, the observations were added at 06 UTC and 18 UTC of each day for assimilation and then forecast 24 h. The physical parameterizations of the model and the comparison test group remained consistent with the single-case experiment.

4. Results

4.1. Analysis of Assimilation Data

From Figures 4 and 5, it can be seen that the FY3D satellite data of 1800 UTC on 1 July in the Beijing area are all clear-sky data. Figure 9 shows the geographical distribution of MWR observations, retrieval data, and clear-sky observations in the Beijing area at the 850 hPa (Figure 9a) and 500 hPa (Figure 9b) levels at 0600 UTC on 2 July. In the Beijing region, there are three profiles of radiation retrieval from the cloud region of FY3D, with clear-sky data primarily distributed to the northeast. Figure 10 displays the retrieval temperature and humidity profiles alongside MWR profiles from adjacent locations. The adjacent MWR sites are numbered 54399, 54419, and 54597 respectively. From the profile plots, it can be observed that there is a significant correlation between the retrieval profiles and the MWR data, thus validating the effectiveness of cloud area radiation data retrieval.

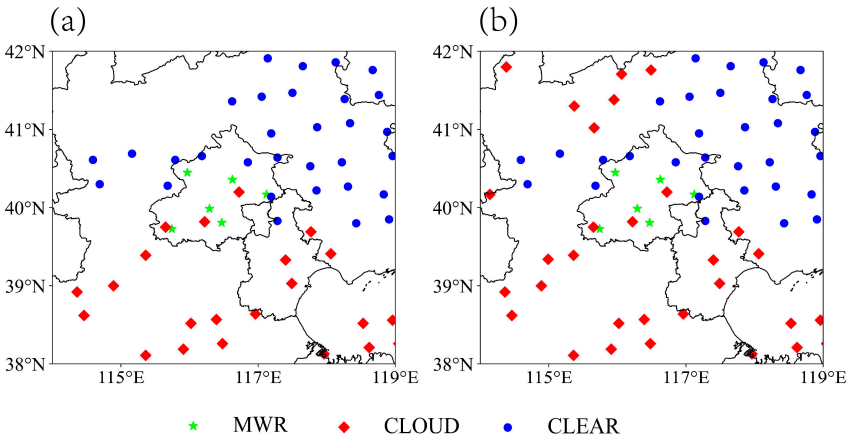

Figure 9. MWR, retrieval, and clear-sky observations at (**a**) 850 hPa and (**b**) 500 hPa in Beijing at 0600 UTC on 2 July 2021.

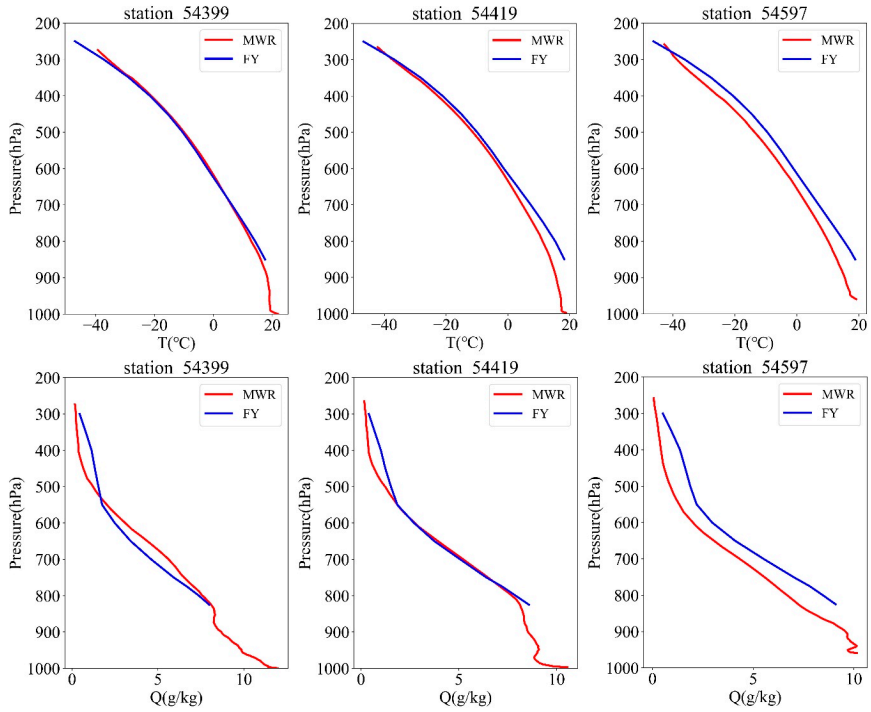

Figure 10. Temperature and humidity profiles for the MWR, along with its adjacent MWTS-2/WMHS-2 cloud area retrievals from sites 54399, 54419, and 54597 at 0600 UTC on 2 July 2021.

Table 2 shows the number of clear-sky scan bins and retrieval data under cloudy conditions of MWTS-2 and MWHS-2 assimilated at 18 and 06 UTC. The amount of retrieval data for temperature and humidity is consistent. For clear-sky radiance data, MWTS-2 has more scan bins compared with MWHS-2 because more MWTS-2 channels were used than MWHS-2 channels. Additionally, the weighting function peak heights for channels 8 and 9 of MWTS-2 are above 90 hPa, making them less affected by the surface and cloud, thus retaining more data. For this case study, at both 18 and 06 UTC, the amount of clear-sky data and retrieval data under cloudy conditions is comparable. Notably, at 18 UTC on 1 July, the number of retrieval data points under cloudy conditions exceeds that of the clear-sky scan points. This highlights the importance of observations under cloudy conditions, demonstrating that effectively utilizing such data can increase the utilization rate of satellite data. It also indicates that, in this case study, both clear-sky and cloudy data impact the experiment.

Table 2. Amount of retrieval data and clear-sky radiance.

Cycle Time	Amount of Retrieval Data	Amount of Clear-Sky Radiance	
		Scan Bins of MWTS-2	Scan Bins of MWHS-2
18 UTC	2307	1587	420
06 UTC	2196	1960	551

4.2. Impact on Analysis Increment

MWTS-2/MWHS-2 and ground-based microwave radiometers mainly affect mode temperature and humidity. To evaluate the influence of different datasets on the analysis field, we analyze the adjustment effects on the analysis field and their contributions to the initiation and development of precipitation, focusing on specific humidity increments at the initial assimilation time. The analysis includes vertical cross-sections of specific humidity increments (Figure 11) and the 500 and 800 hPa humidity increment fields (Figure 12) for four assimilation experiments around Beijing at 1800 UTC on 1 July.

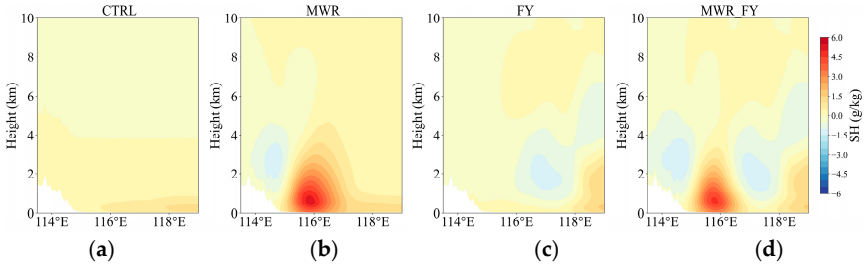

Figure 11. Vertical cross-sections of the specific humidity increments after the first data assimilation along 40°N from (**a**) CTRL, (**b**) MWR, (**c**) FY, and (**d**) MWR_FY.

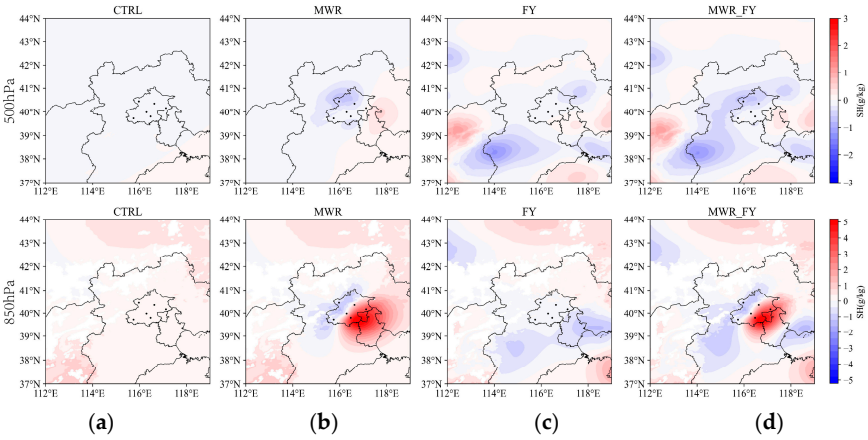

Figure 12. Specific humidity increments after the first data assimilation at 500 hPa and 850 hPa altitude from (**a**) CTRL, (**b**) MWR, (**c**) FY, and (**d**) MWR_FY, with the black mark indicating the location of the ground-based microwave radiometer station.

Both the cross-sectional and pressure plane diagrams indicate that the increments in the CTRL experiment are very slight, suggesting a minimal influence of conventional observations at the initial assimilation time on the analysis field. The cross-section of the MWR experiment reveals both positive and negative increments in the 0–4 km altitude range above the Beijing region, with the central value of positive increments surpassing that of negative increments. Similarly, clear positive and negative increment pairs are discernible in the increment diagrams at 500 and 800 hPa altitudes.

The FY experimental vertical cross-section shows that, above the Beijing area, it primarily exhibits small negative humidity increments. Surrounding the Beijing area, both positive and negative increments are simultaneously present, with increment center values smaller than those of the MWR experiment. The data impacting the Beijing area in the FY

experiment at 1800 UTC on 1 July mainly consist of satellite clear-sky radiation data. This suggests that the clear-sky and cloudy data from MWTS-2/MWHS-2 influence the analysis field, albeit to a lesser extent than the ground-based microwave radiometer data in the Beijing region. The increment patterns in the MWR_FY experiment resemble those in the MWR experiment. Although the MWTS-2/MWHS-2 data are more abundant compared with the ground-based microwave radiometer data, in this rainfall case, the increments generated by the ground-based microwave radiometer in the Beijing area are larger than those from MWTS-2/MWHS-2. Therefore, compared with the MWR experiment, the FY experiment shows less noticeable increments in the Beijing region. However, outside the Beijing area, the increments from the MWTS-2/MWHS-2 data are more significant.

Analysis of humidity increments reveals that ground-based microwave radiometers exert a significant influence in the Beijing area. Negative humidity increments to the west of Beijing might inhibit precipitation occurrence, while positive increments to the east could potentially promote precipitation. Through joint assimilation, under the influence of both ground-based microwave radiometers and MWTS-2/MWHS-2 data, adjustments are made across the entire study area.

4.3. Impact on Forecasts

4.3.1. Temperature Prediction Field

To better evaluate the influence of ground-based microwave radiometer and MWTS-2/MWHS-2 data on the model forecast, the temperature forecast field of 500 hPa at 0000 UTC on 3 July is selected for analysis. Figure 13b–e display the overlaid forecasts fields of temperature and wind at 500 hPa altitude for each experiment in Beijing and its surrounding areas at 0000 UTC on 3 July, while Figure 13a shows the GFS analysis field in the same situation. The temperature exhibits a decreasing trend from southeast to northwest, with relatively parallel isotherms. The temperature fields of the four assimilation experiments and the GFS analysis field show a similar distribution pattern, and the flow trends of the wind fields are also similar. However, there are slight differences in the distribution of each experiment group. In the CTRL experiment, the distribution of isotherms in the Beijing area is relatively sparse, with almost the entire Beijing region falling within the range of 264 K and 265 K isotherms. In contrast, the isotherms in the Beijing area for the other three experiments are denser, providing corresponding temperature conditions for precipitation in the Beijing area. Additionally, compared with the CTRL experiment, the experiments incorporating microwave data exhibit temperature distributions in the Beijing area that are closer to the GFS analysis field, with the temperature and wind fields in the MWR_FY experiment being the closest to the GFS.

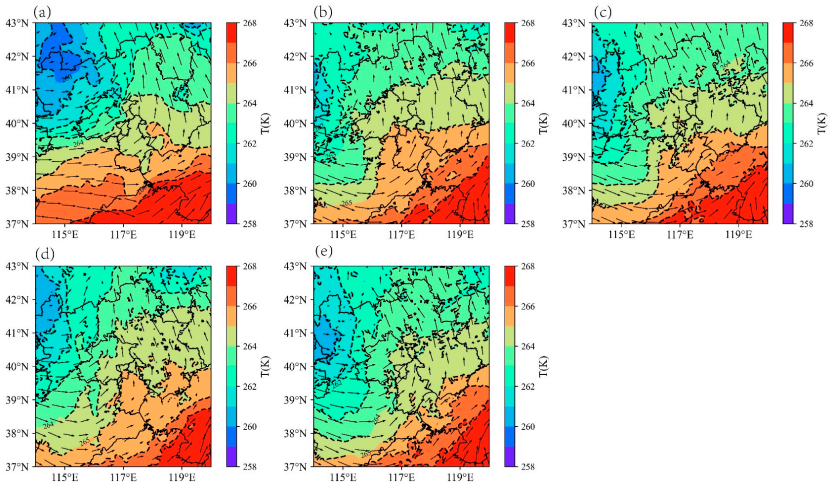

Figure 13. Temperature and wind superposition at 500 hPa forecast field from (**a**) GFS, (**b**) CTRL, (**c**) MWR, (**d**) FY, and (**e**) MWR_FY at 0000 UTC on 3 July 2021. The shadow represents the temperature distribution and the dashed line represents the temperature isotherm.

4.3.2. Humidity Prediction Field

To further investigate the impact of data assimilation on the occurrence and development of severe convective storms, this study analyzed the humidity forecast fields crucial for precipitation. Figure 14 shows vertical cross-sections along 40°N of three meteorological elements—relative humidity, temperature, and wind fields—at 0000 UTC on 3 July 2021. Figure 14a represents the GFS analysis field, while Figure 14b–e show forecast fields from four assimilation experiments. The GFS analysis field indicates that relative humidity reaches 85% from the surface to 400 hPa in the region of 116–120°E, suggesting abundant moisture conducive to precipitation. Further examination of wind field cross-sections from assimilation experiment forecasts reveals strong airflow disturbances and uplift from near the surface to the mid-upper troposphere, facilitating precipitation. By 0000 UTC on 3 July, the precipitation center shifts to the Beijing–Tianjin–Hebei junction. Therefore, relative humidity above 115–116°E is relatively low, with humidity distributions in the FY and MWR_FY experiments better aligning with observations. Compared with the CTRL experiment, the MWR experiment shows smaller adjustments. The FY and MWR_FY experiments exhibit larger adjustment magnitudes. From the overall distribution shape of the humidity cross-section, the MWR_FY experiment best matches the GFS analysis field.

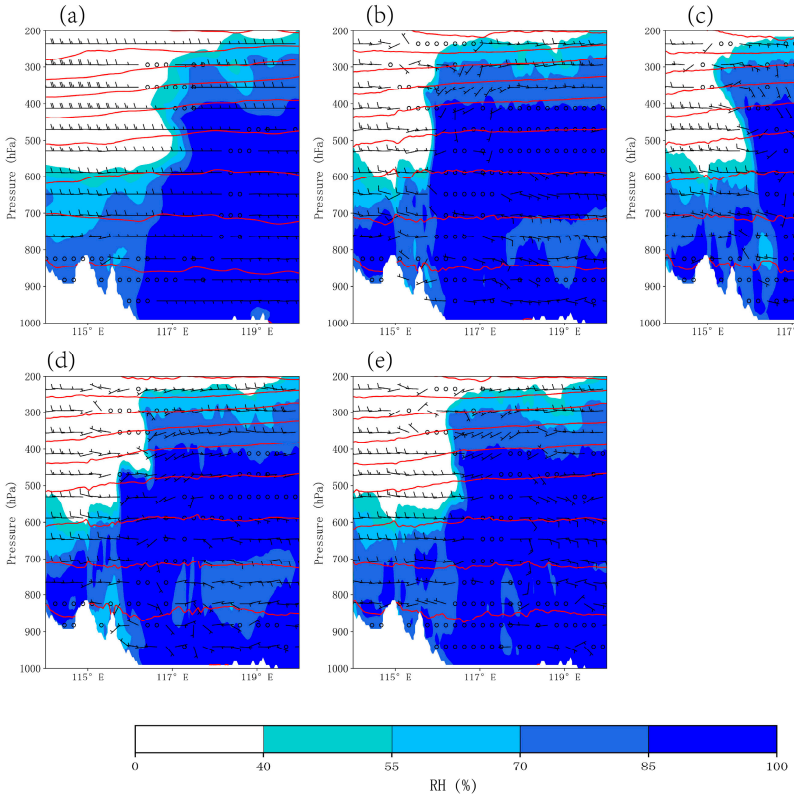

Figure 14. Vertical cross-sections of relative humidity (shadow), temperature (red lines), and wind field (vectors) along 40°N from (**a**) GFS, (**b**) CTRL, (**c**) MWR, (**d**) FY, and (**e**) MWR_FY at 0000 UTC on 3 July 2021.

4.3.3. Precipitation Forecast

Figure 15 shows the accumulated precipitation distributions of actual observations and four experiments over six hours (from 1800 UTC to 2100 UTC on 2 July), the first three hours (from 1800 UTC to 2100 UTC on 2 July), and the last three hours (from 2100 UTC on 2 July to 0000 UTC on 3 July). The cumulative precipitation distribution over six hours shows that the precipitation center of the CTRL experiment is mainly distributed west of Beijing, with a northwest-to-southeast orientation of the rain belt. The MWR experiment effectively adjusts the orientation of the rain belt, aligning it with observations over Beijing, although the precipitation position is slightly westward compared with the actual observations. The

FY experiment's precipitation position is close to the actual observations, but there is false precipitation outside the Beijing area. The MWR_FY experiment overall shows three rain bands, with their pattern closest to the actual observations, and the center of precipitation within the Beijing area consistent with the actual observations, just slightly smaller in terms of precipitation magnitude.

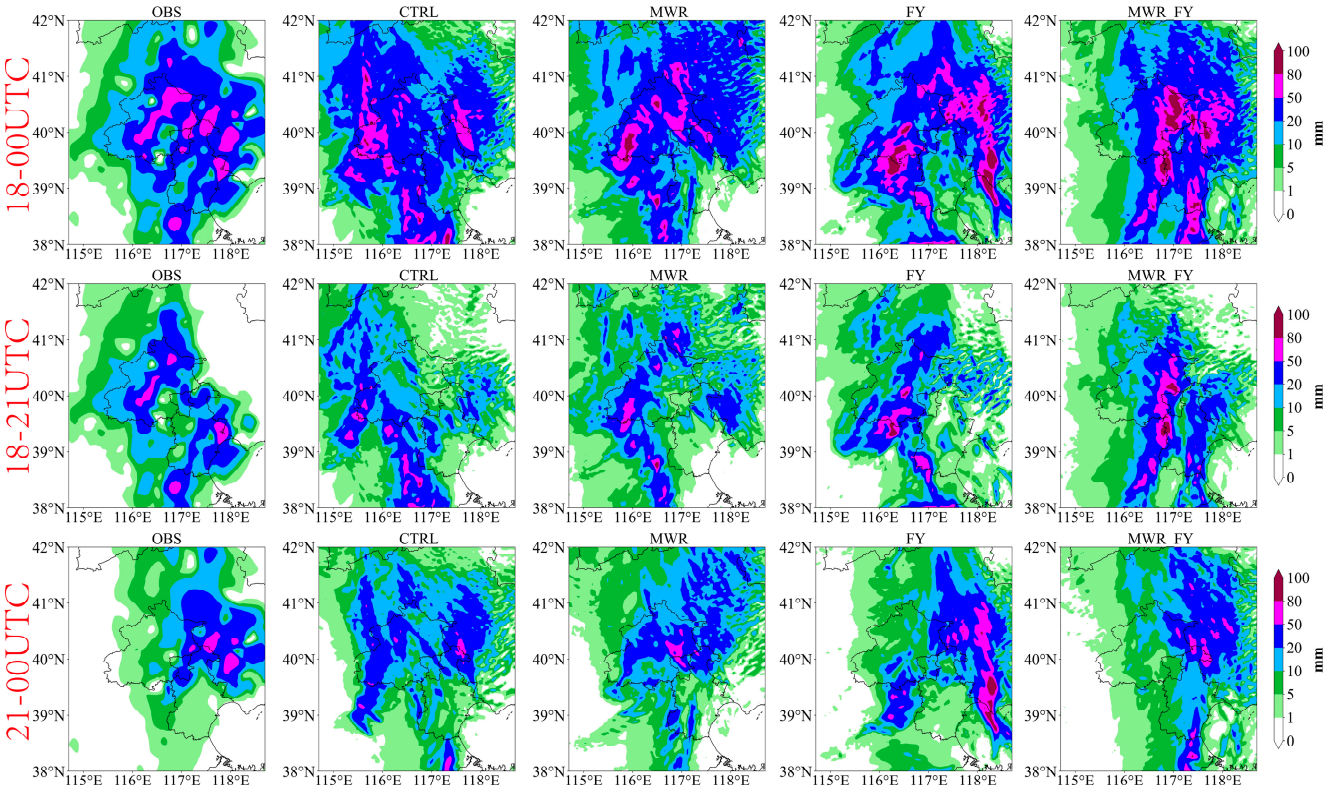

Figure 15. Distribution of precipitation forecasts for the 6 h (from 1800 UTC on 2 July to 0000 UTC on 3 July), the first 3 h (from 1800 UTC to 2100 UTC on 2 July), and the last 3 h (from 2100 UTC on 2 July to 0000 UTC on 3 July) from OBS (actual observation), the CTRL, the MWR, the FY, and the MWR_FY experiments.

Compared with the CTRL experiment, the precipitation distribution over the first three hours reveals notable improvements in precipitation locations for the other three experiments. Specifically, the precipitation center of the MWR experiment is slightly westward within the Beijing area, while the precipitation centers of the FY and MWR_FY experiments are closest to the actual observations. While the MWR_FY experiment exhibits a smaller coverage of heavy rainfall and above compared with the actual observations, its overall precipitation distribution and pattern closely resemble the truth. The accumulated precipitation of the last three hours shows that, compared with the CTRL and MWR experiments, the precipitation at the junction of Beijing, Tianjin, and Hebei in the FY and MWR_FY experiments is closer to the actual observations.

To further explore the impact of data assimilation on precipitation forecast, the threat score (TS) is calculated for the precipitation forecasts of Beijing and its surrounding areas from the four experiments. Figure 16 shows the cumulative precipitation's TS over 6 h (Figure 16a), the first 3 h (Figure 16b), and the last 3 h (Figure 16c). In the 6 h TS, since the precipitation areas of all experiments cover the range of the truth, there is not much difference in TS below the 10 mm level, but differences are evident at the 25 mm and 50 mm levels. At the 25 mm level, compared with the CTRL, the TSs of the other three experiments show significant improvements, with the highest TS observed in the MWR experiment, followed by the MWR_FY. At the 50 mm level, the MWR_FY shows the highest

TS. Assimilating MWR and MWTS-2/MWHS-2 separately results in a slight decrease in TS at the 50 mm level, but a significant improvement is observed after joint assimilation.

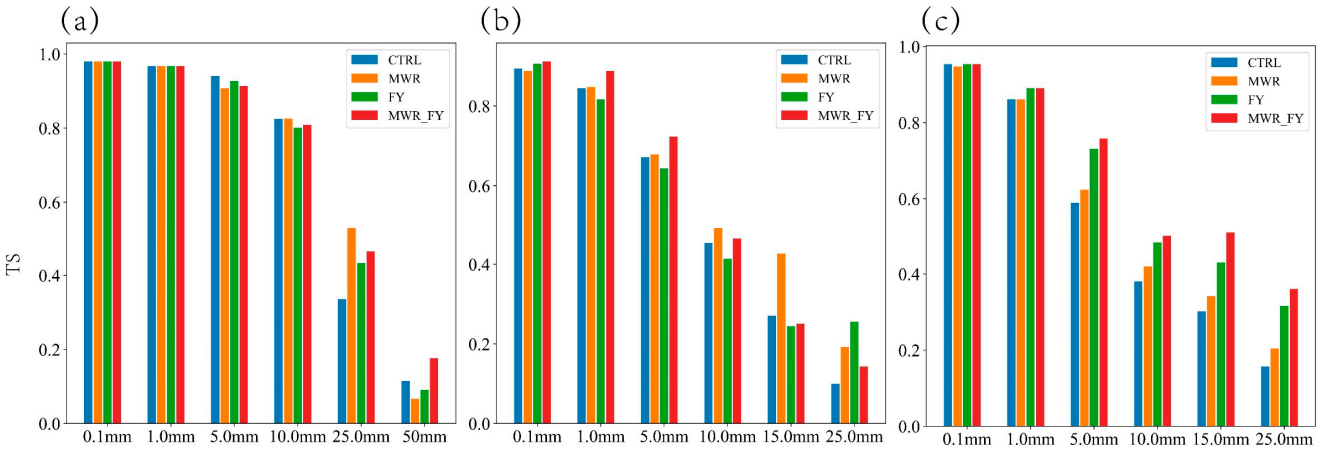

Figure 16. Threat score (TS) for (**a**) 6 h rainfall forecast, (**b**) the first 3 h rainfall forecast, and (**c**) the last 3 h rainfall forecast from all four experiments at different rainfall thresholds.

In the first 3 h scores, the most significant improvements in the MWR experiment are observed at the 10 mm and 15 mm levels, while, for the FY experiment, the most notable improvement is seen at the 25 mm level. The joint assimilation experiment (MWR_FY) shows a lower TS for heavy rainfall levels (>25 mm) in the first 3 h compared with individual assimilation experiments. However, its improvements in precipitation location and pattern are significant, with a higher TS observed for precipitation levels of 10 mm and below. For the last three-hour TS, the MWR_FY's is highest, followed by the FY experiment. Overall, in this six-hour short-term heavy rainfall case, compared with the CTRL experiment forecast, the assimilation of ground-based microwave radiometer data contributes slightly more to the accuracy of precipitation forecasts in the first three hours, whereas the assimilation of MWTS-2/MWHS-2 data has a slightly greater contribution in the latter three hours. The joint assimilation of these datasets further enhances the prediction of the entire rainfall band, particularly regarding the pattern and location of precipitation.

4.4. Prediction Results of Batch Experiment

To verify the impact of the observations on the forecasts, root mean square error and bias (rmse/bias) and precipitation threat scores are used to compare and analyze the results of the batch experiments. As with the single-case experiment, the analyses are carried out mainly for Beijing and the surrounding region. The rmse and bias of temperature and relative humidity variations with height for the 12 h and 24 h forecast fields are calculated using the GFS analyzed field data as the true values and the mean values are calculated for the results of the 10-day experiments.

Figure 17 shows the profiles of the RMSE and bias of temperature and relative humidity for the 12 h and 24 h forecast fields, where (a–d) are temperature and (e–h) are relative humidity. The RMSE values of the 12 h and 24 h forecast fields for temperature and relative humidity for the MWR, FY, and MWR_FY experiments above the 550 hPa altitude show a slight improvement compared with the CTRL experiment but exhibit a slightly negative effect in the lower troposphere. In the bias profiles for temperature above the 750 hPa altitude, the MWR, FY, and MWR_FY experiments are closer to zero compared with the CTRL experiment, with the joint assimilation experiment MWR_FY being the closest to zero. However, there is a negative effect below the 750 hPa altitude. The bias in relative humidity is relatively large, with more pronounced improvements observed in the 12 h forecast field compared with the 24 h forecast field.

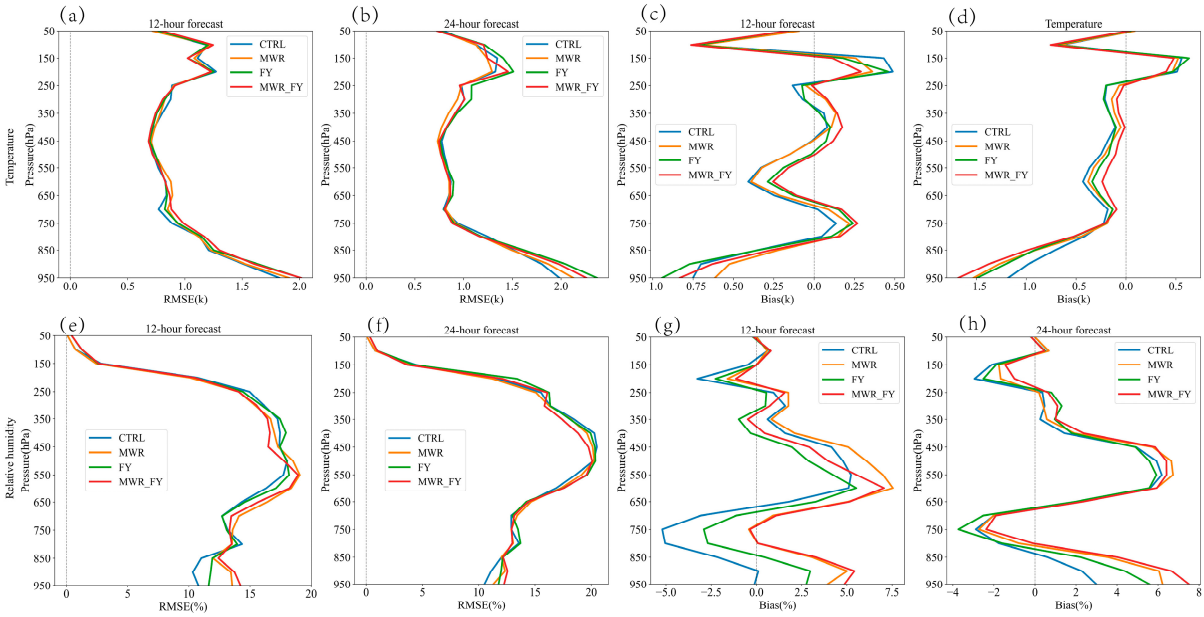

Figure 17. RMSE/bias profiles for 12 h and 24 h temperature (**a**–**d**) and relative humidity (**e**–**h**) forecast fields.

Overall, the improvement effect of microwave data on temperature and relative humidity is mainly observed in the upper-middle troposphere, while it even has a negative effect in the lower-middle troposphere. It may be attributed to the exclusion of some MWTS-2/MWHS-2 data at near-surface heights in this study. Additionally, detection and retrieval accuracies are influenced by factors such as surface topography, leading to errors.

Figure 18 shows the TS scores for the 24 h and 12 h by 12 h precipitation forecasts for the batch experiments. For the 0–12 h precipitation forecasts, the improvement in forecasts from the experiments incorporating microwave observation is neutral to positive. The effect is negative for moderate rainfall and below, but slightly positive for 25 mm and 50 mm. For 12–24 h precipitation forecasts, the other three experiments show slightly significant improvements compared with the CTRL experiment. Among them, the MWR experiment has a more significant improvement compared with the FY experiment, while the MW_FY experiment has a lower TS than the MWR experiment at 10 mm and below level but the highest ratings at 25 and 50 mm levels. In terms of the 24 h forecast, the microwave data assimilation experiment has a very small, if not negative, effect on improving light rain forecasts. However, at 10 mm and above precipitation, the improvement of the assimilated experiments is significant. In particular, the MWR_FY experiment has the largest TS at 10 mm, 25 mm, and 50 mm.

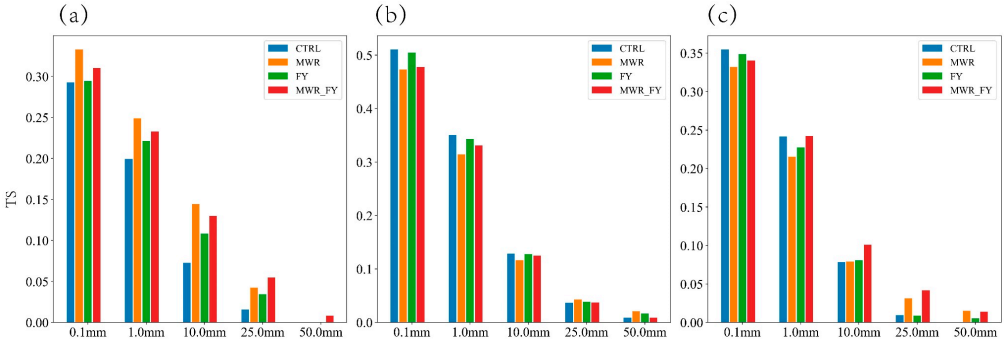

Figure 18. Threat score (TS) for (**a**) 24 h rainfall forecast, (**b**) the first 12 h rainfall forecast, and (**c**) the last 12 h rainfall forecast from all four experiments of 10-days at different rainfall thresholds.

The analysis of the precipitation results from the batch experiments shows that the ground-based microwave radiometer and the FY-3D microwave sounder data have a positive impact on the forecast of short-term precipitation. The effect may be slightly different for different precipitation scenarios, but the overall effect on assimilation and forecast is neutral to positive. It can also be seen that joint assimilation has a further positive effect compared with individual assimilation.

5. Conclusions

This study employed the regional numerical weather forecast model WRF and the WRFDA assimilation system to assimilate ground-based microwave radiometer and FY-3D MWTS-2/MWHS-2 observation. Both separate assimilation and joint assimilation experiments were conducted to compare and analyze the forecasting performance of a short-duration heavy rainfall event in the Beijing region. Further 10-day batch experiments were used to verify the impact of the two microwave observations on temperature, humidity, and precipitation forecasts. The main conclusions were as follows.

(1) The utilization of retrieval methods for cloud observation increases the utilization rate of satellite data. Analysis increment indicates that both clear-sky radiance data from MWTS-2/MWHS-2 and temperature and humidity profiles retrieved from cloudy regions contribute to the improvement of the analysis field. The conventional observations' effects are not significant, the ground-based microwave radiometer data mainly affect the Beijing region, while the FY-3D data can impact the entire experimental area. This reflects that the ground-based microwave radiometer and FY3D data can compensate for the inadequacy of conventional observations.

(2) Compared with the CTRL experiments, the other three sets of experiments show a slight improvement in forecasting precipitation from the single-case experiment. In the 6 h accumulated precipitation, the MWR_FY experiment improves the TS by 38.2% and 54.4% at the 25 mm and 50 mm levels, respectively, compared with the CTRL experiment. The ground-based microwave radiometer and MWTS-2/MWHS-2 data exhibit effective adjustment on the thermal structure of the analysis field, which is one of the reasons to improve the accuracy of precipitation forecasting. For this rainfall case, the forecasting of the joint assimilation is closest to the actual observations.

(3) From the results of the temperature and humidity forecasts of the batch experiments, it is clear that the ground-based microwave radiometer and MWTS-2/MWHS-2 have an improving effect at heights above the upper-middle troposphere, and that the joint assimilation of the two types of observations has relatively the best improving effect among the experiments. However, there is a slightly negative effect at some heights. The analysis of the TS from precipitation forecasts confirms that the addition of the two types of microwave data improves the accuracy of the forecasts for larger amounts of precipitation.

In this study, despite assimilating effectively the ground-based microwave radiometer and FY-3D MWTS-2/MWHS-2 clear-sky radiance and cloud-sky retrieval data, these two types of data remain challenging for forecasting severe convective weather, particularly the assimilation of all-sky satellite data. While joint assimilation shows the overall best performance in predicting rainfall bands in this study case, there is a reduction in the intensity at the center of heavy rainfall. This necessitates further investigation into the physical effects of the data on the assimilation system, which could be achieved through case studies and further physical research. For the batch experiments where the rmse and bias profiles show negative effects at some heights, this needs to be examined for the observations at these heights, and further research is required. Additionally, this study only addresses the weather conditions of precipitation. To more comprehensively reveal the impact of the two types of data on assimilation and forecasting, future work should extend to cases involving typhoons, cold waves, and severe convective weather.

Author Contributions: Conceptualization, W.C. and B.W.; methodology, Z.J. and B.W.; data curation, S.W., S.F., J.M. and Z.Y.; writing—original draft preparation, B.W.; writing—review and editing, W.C., Y.B. and G.P.P. All authors have read and agreed to the published version of the manuscript.

Funding: This research was funded by the Natural Science Foundation of China (Grant no. U2242212), the Second Tibetan Plateau Scientific Expedition and Research (STEP) program (Grant no. 2019QZKK0105), the Fengyun Satellite Application Pilot Program (2022) Xu Jianmin Meteorological Satellite Innovation Center Special Project (Grant no. FY-APP-ZX-2022.0208), the Major Science and Technology Program of the Ministry of Water Resources of China (Grant no. SKS-2022072), and the Water Science and Technology Project of Jiangsu Province (Grant no. 2023022).

Data Availability Statement: The original contributions presented in the study are included in the article, further inquiries can be directed to the corresponding author.

Acknowledgments: The authors acknowledge the funding supporters and the data providers for the research support and help. Authors are also grateful to the anonymous reviewers for their feedback and constructive comments that resulted in improving the initially submitted manuscript.

Conflicts of Interest: The authors declare no conflict of interest.

References

1. Xu, L.; Cheng, W.; Deng, Z.; Liu, J.; Wang, B.; Lu, B.; Wang, S.; Dong, L. Assimilation of the FY-4A AGRI clear-sky radiance data in a regional numerical model and its impact on the forecast of the "21·7" Henan extremely persistent heavy rainfall. *Adv. Atmos. Sci.* **2023**, *40*, 920–936. [CrossRef]
2. Geer, A.J.; Lonitz, K.; Weston, P.; Kazumori, M.; Okamoto, K.; Zhu, Y.; Liu, E.H.; Collard, A.; Bell, W.; Migliorini, S.; et al. All-sky satellite data assimilation at operational weather forecasting centres. *Q. J. R. Meteorol. Soc.* **2018**, *144*, 1191–1217. [CrossRef]
3. Le, M.H.; Zhang, R.; Nguyen, B.Q.; Bolten, J.D.; Lakshmi, V. Robustness of gridded precipitation products for Vietnam basins using the comprehensive assessment framework of rainfall. *Atmos. Res.* **2023**, *293*, 106923.
4. Zhu, Y.; Liu, E.; Mahajan, R.; Thomas, C.; Groff, D.; Van Delst, P.; Collard, A.; Kleist, D.; Treadon, R.; Derber, J.C. All-sky microwave radiance assimilation in NCEP's GSI analysis system. *Mon. Weather Rev.* **2016**, *144*, 4709–4735. [CrossRef]
5. Xu, D.; Min, J.; Shen, F.; Ban, J.; Chen, P. Assimilation of MWHS radiance data from the FY-3B satellite with the WRF Hybrid-3DVAR system for the forecasting of binary typhoons. *J. Adv. Model. Earth Syst.* **2016**, *8*, 1014–1028. [CrossRef]
6. Li, J.; Li, J.L.; Otkin, J.; Schmit, T.J.; Liu, C.Y. Warning information in a preconvection environment from the geostationary advanced infrared sounding system—A simulation study using the IHOP case. *J. Appl. Meteorol. Climatol.* **2011**, *50*, 776–783. [CrossRef]
7. Okamoto, K. Evaluation of IR radiance simulation for all-sky assimilation of Himawari-8/AHI in a mesoscale NWP system. *J. Appl. Meteorol. Climatol.* **2017**, *143*, 1517–1527. [CrossRef]
8. Bauer, P.; Geer, A.J.; Lopez, P.; Salmond, D. Direct 4D-Var assimilation of all-sky radiances. Part I: Implementation. *Q. J. R. Meteorol. Soc.* **2010**, *136*, 1868–1885. [CrossRef]
9. Zhang, T.; Bao, Y.S.; Lu, Q.F. The Iasi date assimilating experiments on the heavy rain over the Yangtze river basin. *Sci. Technol. Eng.* **2016**, *16*, 9–16+36.
10. Dou, F.L.; Lu, Q.F.; Guo, Y. Overview of Researches on All-Sky Satellite Microwave Data Variational Assimilation. *Adv. Earth Sci.* **2019**, *34*, 1120–1130.
11. Kelly, G.; Thépaut, J.N. Evaluation of the impact of the space component of the Global Observing System through Observing System Experiments. *ECMWF Newsl.* **2007**, *113*, 16–28.
12. Gu, S.Q.; Wang, Z.H.; Weng, F.Z.; Jishan, X.; Peiming, D. A study for improving a microwave land surface emissivity model with NOAA/AMSU data and the Grapes 3Dvar system. *Plateau Meteorol.* **2006**, *25*, 1101–1106.
13. Liu, Z.; Schwartz, C.S.; Snyder, C.; Ha, S.Y. Impact of assimilating AMSU-A radiances on forecasts of 2008 Atlantic tropical cyclones initialized with a limited-area ensemble Kalman filter. *Mon. Weather Rev.* **2012**, *140*, 4017–4034. [CrossRef]
14. Zhang, L.H.; Shen, T.L.; Wang, H.L. Variational assimilation of AMSU data and its application to Numerical simulation of heavy rainfall. *Plateau Meteorol.* **2007**, *26*, 1004–1012.
15. Carminati, F.; Migliorini, S. All-sky data assimilation of MWTS-2 and MWHS-2 in the Met Office global NWP system. *Adv. Atmos. Sci.* **2021**, *38*, 1682–1694. [CrossRef]
16. Lu, Q.F. Initial evaluation and assimilation of FY-3A atmospheric sounding data in the ECMWF System. *Sci. China Earth Sci.* **2011**, *54*, 1453–1457. [CrossRef]
17. Lu, Q.F.; Bell, W.; Bauer, P.; Bormann, N.; Peubey, C. An evaluation of FY-3A satellite data for numerical weather prediction. *Q. J. R. Meteorol. Soc.* **2011**, *137*, 1298–1311. [CrossRef]
18. Zou, X.; Wang, X.; Weng, F.; Li, G. Assessments of Chinese Fengyun Microwave Temperature Sounder (MWTS) Measurements for Weather and Climate Applications. *J. Atmos. Ocean. Technol.* **2011**, *28*, 1206–1227. [CrossRef]
19. Guan, L.; Zou, X.; Weng, F.; Li, G. Assessments of FY-3A microwave humidity sounder measurements using NOAA-18 microwave humidity sounder. *J. Geophys. Res. Atmos.* **2011**, *116*, D10106. [CrossRef]

20. Chen, K.Y.; English, S.; Bormann, N.; Zhu, J. Assessment of FY-3A and FY-3B MWHS observations. *ECMWF Tech. Memo.* **2014**, *734*, 1280–1290. [CrossRef]
21. Lawrence, H.; Bormann, N.; Lu, Q.; Geer, A.; English, S. An evaluation of FY-3C MWHS-2 at ECMWF. *EUMETSAT/ECMWF Fellowsh. Programme Res. Rep.* **2015**, *37*, 1–24.
22. Lu, Q.; Lawrence, H.; Bormann, N.; English, S.; Lean, K.; Atkinson, N.; Bell, W.; Carminati, F. *An Evaluation of FY-3C Satellite Data Quality at ECMWF and the Met Office*; European Centre for Medium-Range Weather Forecasts: Reading, UK, 2015.
23. Sun, W.; Xu, Y. Assimilation of FY-3D MWHS-2 radiances with WRF hybrid-3DVar system for the forecast of heavy rainfall evolution associated with Typhoon Ampil. *Mon. Weather Rev.* **2021**, *149*, 1419–1437. [CrossRef]
24. Xu, D.M.; Shu, A.Q.; Li, H.; Shen, F.; Li, Q.; Su, H. Effects of Assimilating Clear-Sky FY-3D MWHS2 Radiance on the Numerical Simulation of Tropical Storm Ampil. *Remote Sens.* **2021**, *13*, 2873. [CrossRef]
25. Song, L.; Shen, F.; Shao, C.; Shu, A.; Zhu, L. Impacts of 3DEnVar-Based FY-3D MWHS-2 Radiance Assimilation on Numerical Simulations of Landfalling Typhoon Ampil (2018). *Remote Sens.* **2022**, *14*, 6037. [CrossRef]
26. Chen, K.; Chen, Z.; Xian, Z.; Li, G. Impacts of the all-sky assimilation of FY-3C and FY-3D MWHS-2 radiances on analyses and forecasts of typhoon Hagupit. *Remote Sens.* **2023**, *15*, 2279. [CrossRef]
27. Vandenberghe, F.; Ware, R. 4-dimensional variational assimilation of ground-based microwave observations during a winter fog event. In International Symposium on Atmospheric Sensing with GPS; Tsukuba, Japan. 2002. Available online: https://radiometrics.com/wp-content/uploads/2021/10/Vandenberghe_ASGPS-02.pdf (accessed on 15 July 2024).
28. Otkin, J.A.; Hartung, D.C.; Turner, D.D.; Petersen, R.A.; Feltz, W.F.; Janzon, E. Assimilation of surface-based boundary layer profiler observations during a cool-season weather event using an observing system simulation experiment. Part I: Analysis impact. *Mon. Weather Rev.* **2011**, *139*, 2309–2326. [CrossRef]
29. Hartung, D.C.; Otkin, J.A.; Petersen, R.A.; Turner, D.D.; Feltz, W.F. Assimilation of surface-based boundary layer profiler observations during a cool-season weather event using an observing system simulation experiment. Part II: Forecast assessment. *Mon. Weather Rev.* **2011**, *139*, 2327–2346. [CrossRef]
30. Caumont, O.; Cimini, D.; Löhnert, U.; Alados-Arboledas, L.; Bleisch, R.; Buffa, F.; Ferrario, F.E.; Haefele, A.; Huet, T.; Madonna, F. Assimilation of humidity and temperature observations retrieved from ground-based microwave radiometers into a convective-scale NWP model. *Q. J. R. Meteorol. Soc.* **2016**, *142*, 2692–2704. [CrossRef]
31. Martinet, P.; Cimini, D.; De Angelis, F.; Canut, G.; Unger, V.; Guillot, R.; Tzanos, D.; Paci, A. Combining ground-based microwave radiometer and the AROME convective scale model through 1DVAR retrievals in complex terrain: An Alpine valley case study. *Atmos. Meas. Tech. Discuss.* **2017**, *10*, 3385–3402. [CrossRef]
32. Martinet, P.; Cimini, D.; Burnet, F.; Ménétrier, B.; Michel, Y.; Unger, V. Improvement of numerical weather prediction model analysis during fog conditions through the assimilation of ground-based microwave radiometer observations: A 1D-Var study. *Atmos. Meas. Tech.* **2020**, *13*, 6593–6611. [CrossRef]
33. Vural, J.; Merker, C.; Löffler, M.; Leuenberger, D.; Schraff, C.; Stiller, O.; Schomburg, A.; Knist, C.; Haefele, A.; Hervo, M. Improving the representation of the atmospheric boundary layer by direct assimilation of ground-based microwave radiometer observations. *Q. J. R. Meteorol. Soc.* **2024**, *150*, 1012–1028. [CrossRef]
34. Qi, Y.; Fan, S.; Li, B.; Mao, J.; Lin, D. Assimilation of ground-based microwave radiometer on heavy rainfall forecast in Beijing. *Atmosphere* **2021**, *13*, 74. [CrossRef]
35. Qi, Y.; Fan, S.; Mao, J.; Li, B.; Guo, C.; Zhang, S. Impact of assimilating ground-based microwave radiometer data on the precipitation bifurcation forecast: A case study in Beijing. *Atmosphere* **2021**, *12*, 551. [CrossRef]
36. Wenying, H.; Chen, H.; Li, J. Influence of assimilating ground-based microwave radiometer data into the WRF model on precipitation. *Atmos. Ocean. Sci. Lett.* **2020**, *13*, 107–112.
37. Liu, X.; Liu, D.; Guo, L. The observational precision of domestic MWP967KV ground-based microwave radiometer. *J. Appl. Meteorol. Sci.* **2019**, *30*, 731–744.
38. Xu, H.; Zhang, X.F.; Huang, S.Y.; Fu, W. Comparative analysis of observation data between ground-based microwave radiometer and UAV Attached radiosonde. *Bull. Sci. Technol.* **2020**, *36*, 48–53.
39. Xu, J.; Qiao, H.; Zhou, H.G.; Zhang, Y.Y.; Wu, Y.X. Comparison and case analysis of temperature and humidity between Airda-HTG4 ground-based multi-channel microwave radiometer and sounding station. *Meteorol. Hydrol. Mar. Instrum.* **2023**, *40*, 12–15.
40. Hersbach, H.; Bell, B.; Berrisford, P.; Hirahara, S.; Horányi, A.; Muñoz-Sabater, J.; Nicolas, J.; Peubey, C.; Radu, R.; Schepers, D. The ERA5 global reanalysis. *Q. J. R. Meteorol. Soc.* **2020**, *146*, 1999–2049. [CrossRef]
41. Xian, Z.; Chen, K.; Zhu, J. All-sky assimilation of the MWHS-2 observations and evaluation the impacts on the analyses and forecasts of binary typhoons. *J. Geophys. Res. Atmos.* **2019**, *124*, 6359–6378. [CrossRef]
42. Li, J.; Liu, G. Direct assimilation of Chinese FY-3C microwave temperature sounder-2 radiances in the global GRAPES system. *Atmos. Meas. Tech.* **2016**, *9*, 3095–3113. [CrossRef]
43. Carminati, F.; Atkinson, N.; Candy, B.; Lu, Q. Insights into the microwave instruments onboard the Fengyun 3D satellite: Data quality and assimilation in the Met Office NWP system. *Adv. Atmos. Sci.* **2021**, *38*, 1379–1396. [CrossRef]
44. Auligné, T.; Anthony, P. Adaptive bias correction for satellite data in a numerical weather prediction system. *Q. J. R. Meteorol. Soc. A J. Atmos. Sci. Appl. Meteorol. Phys. Ocean.* **2007**, *133*, 631–642. [CrossRef]

45. Milstein Adam, B.; William, J. Neural network temperature and moisture retrieval algorithm validation for AIRS/AMSU and CrIS/ATMS. *J. Geophys. Res. Atmos.* **2016**, *121*, 1414–1430. [CrossRef]
46. Bao, Y.S.; Wang, Z.J.; Chen, Q.; Zhou, A.M.; Dong, Y.H.; Min, J.Z. Preliminary study on atmospheric temperature profiles retrieval from GIIRS based on FY-4A satellite. *Aerosp. Shanghai* **2017**, *34*, 28–37.
47. Jin, Z.Q.; Zhang, H.; Bao, Y.S.; Cheng, W.; Cui, W.; Guan, Y.H.; Li, H.; Mao, J.J. Experimental research of FY-3D microwave detector cloudy data assimilation based on Temperature and humidity profile retrieval. *Sci. Technol. Eng.* **2023**, *23*, 5429–5443.
48. Zhao, W.; Sun, J. Analysis of the July 2021 atmospheric circulation and weather. *Meteorol. Mon.* **2021**, *47*, 1289–1296.
49. Hong, S.Y.; Lim, J.O.J. The WRF single-moment 6-class microphysics scheme (WSM6). *Asia-Pac. J. Atmos. Sci.* **2006**, *42*, 129–151.
50. Mlawer, E.J.; Taubman, S.J.; Brown, P.D. Radiative transfer for in homogeneous atmospheres: RRTM, a validated correlated-k model for the longwave. *J. Geophys. Res. Atmos.* **1997**, *102*, 16663–16682. [CrossRef]
51. Chou, M.D.; Suarez, M.J. An Efficient Thermal Infrared Radiation Parameterization for Use in General Circulation Models. *NASA Tech. Memo.* **1994**, *3*, 104606.
52. Tewari, M.; Chen, F.; Wang, W.; Dudhia, J.; LeMone, M.A.; Mitchell, K.; Ek, M.; Gayno, G.; Wegiel, J.; Cuenca, R.H. Implementation and verification of the Unified NOAH land surface model in the WRF model. In Proceedings of the 20th Conf. on Weather Analysis and Forecasting/16th Conf. on Numerical Weather Prediction, Seattle, WA, USA, 12–16 January 2004; pp. 11–15.
53. Foken, T. 50 years of the Monin-Obukhov similarity theory. *Bound. Layer Meteorol.* **2006**, *119*, 431–447. [CrossRef]
54. Kain, J.S. The Kain-Fritsch convective parameterization: An update. *J. Appl. Meteorol.* **2004**, *43*, 170–181. [CrossRef]
55. Wu, W.S.; Purser, R.J.; Parrish, D.F. Three-dimensional variational analysis with spatially inhomogeneous covariances. *Mon. Weather Rev.* **2002**, *130*, 2905–2916. [CrossRef]